Influence of Irregular Coastlines on a Tornadic Mesovortex in the Pearl River Delta during Monsoon Season. Part II: Numerical Experiments

Lanqiang Bai*[1], Dan Yao*[2], Zhiyong Meng[3], Yu Zhang[4], Xianxiang Huang[5], Zhaoming Li[5]

[1] *Foshan Tornado Research Center, and China Meteorological Administration Tornado Key Laboratory, Guangdong Meteorological Service, and Southern Marine Science and Engineering Guangdong Laboratory (Zhuhai), Guangdong, China*

[2] *Meteorological Observation Centre, CMA, Beijing, China*

[3] *Department of Atmospheric and Oceanic Sciences, and China Meteorological Administration Tornado Key Laboratory, School of Physics, Peking University, Beijing, China*

[4] *Guangzhou Meteorological Observatory, CMA, Guangdong, China*

[5] *China Meteorological Administration Tornado Key Laboratory and Foshan Tornado Research Center, CMA, Guangdong, China*

Article Highlights:

• The land–sea contrast of trumpet-shaped coastline is an important component for rotating storm development by producing quasi-stationary wind shift boundaries.

• The intersection zone of cold pool outflows, prevailing and sheared monsoonal onshore flows is characterized by local maxima of ambient vertical vorticity.

• Simulations of rotating storms associated with the land–sea contrast of trumpet-shaped coastline are highly sensitive to both environmental and storm-scale details.

* Corresponding authors: Dr. Lanqiang Bai (bailanqiang@foxmail.com)
Dr. Dan Yao (yaod@cma.gov.cn)

ABSTRACT

As demonstrated in the first part (Part I) of this study, wind-shift boundaries routinely form along the west coast of the Pearl River Delta due to the land–sea contrast of "trumpet" shape coastline in summer monsoon season. It is proposed that the unique topography has played essential roles in the modification of vorticity budget of mesovortex formation. This article (Part II) aims to examine the mesovortex genesis during the 1 June 2020 tornadic event and the roles of the trumpet-shaped coastline through multiple numerical simulations. On mesoscale, the modeling reproduced two mesovortices that were in close proximity in time and space to the realistic mesovortices. In agreement with observations, finger-like echoes preceding hook echoes were also reproduced over the triple point. On storm scale, in addition to the modeled mesovortex over the triple point, another mesovortex originated from an enhanced discrete vortex along airmass boundary via shear instability. Results from sensitivity experiments suggest that simulation of rotating storms in this region is sensitive to local environmental details and storm dynamics. The strengths of cold pool surges from preexisting storms influence the wrap-up of finger-like echoes and the mesovortex formation. Although the simulations did not perfectly mimic the observed processes on storm scale, they provide an opportunity to better understand the genesis of rotating storms in this tornado hotspot. The findings suggest that the trumpet-shaped coastline is an important component for the mesovortex production during the monsoon active season. It is hoped that this study will increase the situational awareness for forecasters regarding the regional nonmesocyclone tornado environments.

Key words: Mesovortex, tornado, land–sea contrast, coastline, monsoon

https://doi.org/10.1007/s00376-023-3096-4

1. Introduction

Tornadoes that are associated with nonmesocyclone process are typically weaker than mesocyclone (or supercell) tornadoes. Nonmesocyclone tornadoes on land are often called landspouts (Bluestein 1985) and occasionally can also be destructive with an intensity of EF2 or EF3 rated on the enhanced Fujita (EF) scale (Wakimoto and Wilson 1989; Yu and Zheng 2020). They often appear in the meso-γ-scale (2–20 km; Orlanski 1975) vortex (i.e., mesovortex; Schenkman and Xue 2016) on the leading edges of squall lines or bow echoes, and sometimes form along surface convergent boundaries such as drylines and fronts (e.g., Houston and Wilhelmson 2007a, b; Lee and Wilhelmson 1997a, b; Schenkman et al. 2012). Prior studies have suggested the difficulty of forecasting the development of nonmesocyclone tornadoes as they usually develop rapidly and often short-lived (Caruso and Davies 2005). Most of these tornadoes have a life cycle of 5–10 min.

Comparing to the supercell tornado environments that are usually characterized by large 0–1-km storm-relative helicity (SRH) and low lifting condensation level (LCL), nonmesocyclone tornadoes frequently occur in an environment with small vertical wind shear and SRH values and/or relatively high LCL heights (Davies 2006). The examined environments for three nonmesocyclone tornadoes in Caruso and Davies (2005) were characterized by overall small near-storm 0–1-km SRH (< 100 $m^2 s^{-2}$). Despite the great forecasting and warning challenges, some environmental ingredients may provide clues for assessing the potential of nonmesocyclone tornado process, such as the steep low-level lapse rates and the high 0–3-km convective available potential energy (CAPE; Rasmussen 2003) along surface convergent boundary (Caruso and Davies 2005). The presence of high low-level CAPE and large lapse rates leads to a high potential for rapid vertical acceleration and thus favors the vertical stretching process.

In contrast with mesocyclone tornadoes, nonmesocyclone tornadoes tend to develop during the early stage of oncoming updrafts (e.g., convective updrafts in storm) while mesocyclone tornadoes tend to be spawned during the mature stage of supercell when the mesocyclone intensifies on lower levels (e.g., Lemon and Doswell 1979; Burgess et al. 1993; Caruso and Davies 2005). Supercell tornadoes are preceded by well-identifiable midlevel mesocyclones on Doppler velocity fields when significant downdrafts have organized in the rear-flank downdraft region. Nonmesocyclone tornadoes are found to be closely associated with low-level circulations that originate from shear instability of surface convergent boundaries. Slow boundary-relative storm motion is typically associated with this type of tornadoes. When storms are positioned over a boundary, the transient vortex via shearing instability on the surface boundary is collocated with vigorous low-level updrafts and thus the environmental vertical vorticity tends to develop deeper and sometimes strengthen to tornadic strength (Wakimoto and Wilson 1989).

Nonmesocyclone tornadoes are not unusual during the convective season in the Pearl River Delta (PRD, "trumpet" shape and concave toward the sea), which is a tornado hotspot in Southern China (Wang 1996; Zhou et al. 2020, 2021; Fan and Yu 2015). For example, the tornadic event occurred over the PRD estuary as presented in the first part of this two-part series (Part I, Bai et al. 2024) was characterized by a mesovortex developing from near-ground level. Part I has presented the observational facts on the multiscale prestorm environments of the tornado that formed in the afternoon on 1 June 2020 when the South China Sea summer monsoon became active (Zhang et al. 2021). This tornado developed in a mesovortex at the southern-end of a quasi-linear convective system (QLCS) in weak tropospheric flows with low shear. Through a series of daily successive numerical simulations over 3 months of June from 2019 to 2021, Part I also has demonstrated that the west coast of PRD is characterized by a quasi-stationary surface convergent boundary that is generally parallel to the coastline. When storm-generated cold outflows interact with this boundary, a source of preexisting enhanced vertical vorticity appears to occur over the boundary intersection area (constituting a triple point). With the fine-resolution observations from an X-band phased-array radar that was located within only 6 km of this tornado, it was found that the initial finger-like echoes that were associated with an intruding gust front developed around the triple point. The finger-like echoes subsequently wrapped up into well-defined hook echoes (Fig. 1) with a midlevel mesovortex signature clearly identified on the Doppler fields. The tornadogenesis was preceded by the occurrence of this mesovortex. Based on the observational facts in Part I, the initial vertical vortex of the midlevel mesovortex is presumed to originate from the ambient vertical vorticity on the triple point.

The increase of understanding on the environmental conditions that support the regional tornadogenesis is an integral part of the disaster prevention and mitigation for severe weather in the PRD region. The purpose of this second part (Part II) is to complement the observational analysis in Part I and explores the possible dynamics of mesovortex formation in the influence of the monsoon, trumpet-shaped coastline, and storm cold outflows by convection-permitting numerical simulations. It is hoped that this study will increase the situational awareness for forecasters regarding the regional nonmesocyclone tornado environments. The rest of this paper is organized as follows. Section 2 describes the model setup and methods. The simulated results from multiple sensitivity experiments are provided in Section 3. Section 4 investigates the genesis of midlevel mesovortex in the control experiment. Summary and discussions are presented in Section 5.

2. Model setup and methods

2.1. Configurations of the control experiment

To obtain insights into the formation processes of the tornadic storm that was associated with multiple airmass boundaries, the fully compressible nonhydrostatic Weather Research and Forecasting (WRF) model, version 3.9.1 (Skamarock et al., 2008), was applied to run high-resolution, dynamically downscaled simulations. Four two-way nested domains were configured using a ratio of 1:3 (Fig. 2a). The outermost domain was designed with a horizontal resolution of 9 km, and the innermost domain was 0.333 km. The vertical extent for the four domains included 50 stretched-grid levels up to 50 hPa on terrain-following coordinates. There were 15 vertical levels configured below 1.2 km above ground level (AGL). Figure 2a presents the land use types around the region of interest. The PRD is characterized by megalopolis and thus its dominant land use type is “urban and built-up” on land. Domains d01, d02 and d03 were initiated at 0800 BJT (Beijing Time = UTC + 8 h) on 1 June 2020 while the innermost domain was initiated at 1000 BJT. All domains were integrated until 2000 BJT on 1 June 2020. The innermost model outputs were saved every 1 min.

Multiple sensitivity tests on microphysical and boundary process parameterization schemes, configuration in large eddy simulation (LES) mode, and the reanalysis data source for initial conditions were also conducted. The simulated results vary in the rain field comparing to the observations. The selected simulation (hereinafter refer to as control experiment) that is most comparable to the observed scenario was driven by the fifth generation of ECMWF atmospheric reanalysis (ERA5) data on pressure level (Hersbach et al. 2020). The ERA5 data are hourly available with a horizontal resolution of 0.25°. The model lateral boundary conditions were updated at an interval of 1 h. The control (CTL) simulation was not configured in LES mode and thus the PBL parameterization scheme was activated using the Yonsei State University (YSU) boundary-layer scheme (Noh et al. 2003). Other physical parameterization schemes include the WRF single-moment 6-class (WSM6) microphysics scheme (Hong and Lim 2006), thermal diffusion land-surface scheme, MM5 Monin-Obukhov surface-layer scheme, RRTM longwave radiation scheme (Mlawer et al. 1997), and Goddard shortwave radiation scheme (Chou and Suarez 1994). The cumulus parameterization option was turned off. The rest settings were configured in defaulted modes.

2.2. Sensitivity experiment by artificial land accretion

Based on the control experiment, a twin experiment was conducted to investigate the influence of the unique land–sea contrast on the formation of rotating storm as discussed in Part I. This sensitivity simulation was designed by changing the PRD sea surface to land surface (hereinafter refer to as CTL-land experiment). Over the PRD sea surface, the dominant land use category (LU_INDEX), land use fraction by category (LANDUSEF), and land mask (LANDMASK) were replaced with the values on the neighboring land surface (Figs. 2c, d). These modifications were conducted in the geographical file “geo_em.d01.nc” during the procedures of WRF Preprocessing System (WPS). Other model settings were completely the same as those in the CTL experiment.

2.3. Sensitivity experiment by cool bubble injection

In addition to the twin simulations, another sensitivity simulation (hereinafter refer to as CTL-bubble experiment) was conducted to investigate the role of storm cold outflow strength in the development of finger-like echoes over the boundary intersection zone as discussed in Part I. A localized volume of negatively buoyant air was placed to the west of the simulated finger-like echoes by modifying the air temperature and temperature tendency in the innermost WRF restart file of CTL experiment at 1220 BJT (a schematic is presented in Fig. 2b). This cool bubble was centered at a height of 1 km (22.7544°N, 113.455°E). It was configured with a horizontal radius of 10 km and a vertical radius of 1.5 km above ground. The potential temperature perturbation was minimized at the center with a minimum perturbation of −10 K and increased to 0 K following a cosine function over a radius of 3.5 km, 6 km and 2 km in the zonal, meridional and vertical directions, respectively. Other settings are the same as the CTL experiment. The method by directly modifying air temperature has been widely applied in idealized simulations (e.g., Bryan and Fritsch 2002; Markowski 2020). By modifying the air temperature, convection initiation is typically accomplished via a warm bubble while cold pool can be generated by adding a cold blob in the initial condition. The associated adjustments of other meteorological variables such as pressure, winds, and specific humidity are expected in a short time period after the model integration. In the current case, the simulated results present changes in a limited zone around the finger-like echoes because the modification in low-level air temperature was conducted in a localized region.

3. Simulated rotating storms from numerical simulations

3.1. Storm-scale overview in the CTL experiment

In this section, the general simulated storm evolutions in the CTL experiment are discussed. To directly compare with the observed storm structures, especially the hook echo signatures (Markowski 2002), the simulated reflectivity at low levels is presented (Fig. 3). Near the location of the realistic tornadogenesis (refer to the cross in Fig. 3), a simulated well-defined hook echo signature was located in the southern-end part of a storm (labeled “Storm A”) since approximately 1240 BJT. In the following 30 min, the appearances of the developing hook echoes became clearer (Fig. 3e).

Given that a model grid spacing of 0.333 km can explicitly resolve convective updrafts, the updraft helicity (UH; Kain et al. 2008) was calculated to assess the midlevel rotating updrafts within storm. Here, the UH was computed by vertically integrating the vertical component of helicity from 2 km to 5 km AGL. Around the hook echo A, distinct local maxima of UH values were recognized, which is indicative of a rotating storm (black isopleths in Fig. 3e). Similar to the observed storm merger, a merger process also occurred in the simulation. As shown in Figs. 3a–d, Storm B, that was located to the south of Storm A, propagated toward the northeast and merged with the hook echoes of Storm A at 1250 BJT. After the disappearance of this supercell-like structure, another distinct hook echo signature (labeled “Hook echo B”) with enhanced UH values was also identified almost at the same location in the following 30 min (e.g., Fig. 3f). These two simulated hook echo signatures are consistent with those described in the observational analysis in Part I.

Near the two hook echo signatures, two columns of enhanced vertical vorticity developed as indicated by the black isosurfaces labeled MV-1 and MV-2 in Fig. 4. The enhanced vertical vorticity of MV-1 (with a value of 0.05 s^{-1}) started from the ground and subsequently reached an altitude of 5.5 km AGL after 1250 BJT (Figs. 4a–c). These vortex signatures are representative of meso-γ-scale vortices rather than tornadoes considering that a grid spacing of 0.333 km can hardly resolve a tornado vortex. To directly compare the rotation with radar observations, a virtual phased-array radar was placed to the south of the simulated Hook echo A. Figure 5 shows that this virtual radar sampled the radial velocities at the 8.1° and 12.0° elevation angles, which were comparable to the X-PAR sampling during this event (Part I). Consistent with the observed mesocyclonic signature, the simulated radial velocities present an evident couplet with a core diameter of approximately 2 km (Fig. 5). This simulated mesocyclonic signature is generally confined in the layer bellow 5 km AGL. Considering that the occurrences of simulated and observed supercell-like storms are in close proximity in time and space, the authors believe the model has faithfully reproduced the general physical processes of rotating storm formation.

3.2. Simulated results with fake land in the PRD

Figure 6 presents the comparisons of low-level reflectivity and dynamic fields between the CTL and CTL-land experiments. With fake land over the original PRD sea surface, the CTL-land experiment failed to generate any mesovortex and supercell-like storm (e.g., Storm A in Fig. 6a). In the absence of the downward branch of sea-breeze circulation, the fake land area was characterized by overall southwesterly monsoonal flows at low levels and thus no triple point is expected in contrast with the realistic scenario (Figs. 6c, d). Additionally, in the absence of PRD sea surface, extra storms developed to the east of the previous Storm A (Fig. 6b). Without the obstruction of the onshore southeasterlies from the original PRD sea surface, the storm cold outflows propagate faster toward the east, which is responsible for the extra storms in the CTL-land experiment (Fig. 6d). Meanwhile, the convergent boundary formed by the storm cold outflows and the onshore flows was located relatively far from the preexisting storms. The resultant displacement between preexisting storms and the enhanced vertical vorticity along the convergent boundary would make it hard to develop mesovortices.

In the current case, the presence of land–sea contrast of the trumpet-shaped coastline overall has decelerated the westerly components by at least 4 m s^{-1} over the northern part of the PRD sea surface (Fig. 7). The twin experiments demonstrate that the trumpet-shaped coastline helps to modify the ambient vertical vorticity budget by perturbing the low-level prevailing monsoonal flows. Such topography-induced perturbations routinely produce surface airmass boundaries in a relatively fixed area. In the presence of other surface boundaries such as storm-generated outflow boundaries or fronts, the resultant triple point would be beneficial to the development of rotating storms. As proposed in Part I, results from the twin experiments suggest an important role does have played by the trumpet-shaped coastline in the regional severe weather.

3.3. Characteristics of simulated convergent boundaries and finger-like echoes

This section provides an overview of the evolution of low-level features that are considered important for the genesis processes of mesovortex in the CTL experiment. The observational evidence discussed in Part I have indicated that the mesovortex formed at the tip of the finger-like echoes over the triple-point zone. In the CTL experiment, the simulated finger-like echoes of Storm A were located in close proximity to the triple point (denoted by the dashed circle in Fig. 8a). This triple point was generated by the convergence of three types of low-level air flows that include storm-generated cold pool outflows (COF), southwesterlies (SW) on land sides, and southeasterlies (SE) over the PRD sea surface (Fig. 8b). The prevailing monsoonal southwesterlies traveled from the cool sea surface to the warm land surface. They were characterized by higher potential temperature in contrast with the sheared monsoonal southeasterlies over the PRD sea surface and the near-ground cold pool outflows that were generated by the preceding storms.

As demonstrated by the long-term numerical simulations in Part I, the land–sea contrast associated with this unique topography generates a meridional surface convergent boundary generally paralleling to the west PRD coast (Fig. 8a). In the afternoon, the downward branch of sea breeze circulation contributes to a tendency of easterly wind component on the sea side of the west coast. On the other hand, greater friction is expected for the low-level airmasses on land side due to the surface roughness contrast. The warmer land surface during the daytime also tends to produce greater decelerations of low-level flows because the heated land strengthens the turbulent exchanges of momentum in the boundary layer. In this case, the heated land surface perturbed the relatively cool maritime airmasses in favor of the development of horizontal convective rolls (HCRs; refer to the band-organized vertical velocity in Fig. 9a). These HCRs intersected with the preexisting meridional surface boundary, producing some local maxima of enhanced vertical vorticity and convergence along the boundary (refer to the thin blue isopleths in Fig. 9).

Closer inspection of the simulated finger-like echoes shows that, in agreement with the observations, they formed on the southern-end part of Storm A near the triple point (Fig. 8a). Recalling the observed analyses based on the X-band phased-array radar and surface weather stations, the realistic mesovortex and triple-point convergence were located in close proximity to the tip of the finger-like echoes (e.g., inset of Fig. 8a). As suggested by the CTL experiment, the triple point was characterized by persistent local maxima of ambient vertical vorticity near the ground (e.g., vortex V1 in Fig. 8). Further investigation suggests that the finger-like echoes were triggered by the enhanced cold outflow surges by the upstream storm (Storm C in Fig. 9b). The simulated wind fields and associated storm morphology resemble the radar observations and the analyzed low-level winds (dashed arrows in the inset of Fig. 8a). Comparing to the observations by the low power phased array radar, the simulated triple point appears an evident signature of radial velocity couplet even in clear sky (Figs. 10a, b). Given the spatial collocation between the triple point and the realistic tornadic mesovortex, the preexisting ambient vertical vorticity over the triple point is presumed to be the initial vortex for the genesis of the realistic mesovortex.

Different from the observations, a reflectivity wrap-up process (i.e., mesovortex formation) did not occur on the simulated finger-like echoes (Fig. 8b). Considering the presence of preexisting ambient vertical vorticity maxima have been located over the triple point, the authors hypothesized that the wrap-up failure was likely a result of limited forced lifting provided by the cold outflow surges from west. In the CTL-bubble sensitivity experiment, with the injected cold air volume as introduced in section 2, the cold pool surges to the west of the finger-like echoes were strengthened (Figs. 2e, f). Figure 10 presents a comparison of simulated radial velocity between the CTL and CTL-bubble experiments around Storm A. The injected cold air volume between Storm C and Storm A produced greater northwesterly components toward the triple point zone (represented by V1 in Fig. 10c) as indicated by the enhanced inbound radial velocity (refer to the dark blue shadings in Figs. 10c, d). Fueled by strong forced lifting when the cold outflow surges interacted with the southeasterlies from the PRD sea surface, the finger-like echoes subsequently wrap-up to be well-defined hook echoes (Fig. 11).

The results from the CTL-bubble sensitivity experiment support the hypothesis that an underestimate of low-level updrafts is a possible cause for the wrap-up failure of finger-like echoes in the CTL experiment. This sensitivity experiment also suggests that the stretching of ambient vertical vorticity over the triple point is sensitive to the cold outflow strength from preexisting storms. On the other hand, recalling the radar observations (inset of Fig. 8a), the cold outflow surges are not that much strong like those in CTL-bubble experiment. This inconsistency may suggest that other equally important factors also contribute to the uncertainty of mesovortex formation on the finger-like echoes, such as the strengths of onshore flows and preexisting vertical vorticity. In the realistic scenario, the updrafts for stretching the ambient vertical vorticity to be a mesovortex are also likely provided by the forced lifting produced by the flow modification owing to the approaching storms that were merging with the observed finger-like echoes. In the simulated scenario, however, there was no merger between the finger-like echoes and any southern approaching storms.

4. Genesis of the simulated mesovortex in the CTL experiment

Although the finger-like echoes in the CTL experiment fails to wrap up and develop a midlevel mesovortex, two mesovortices are still reproduced in close proximity in time and space to the realistic mesovortices (Part I). It suggests a high predictability of mesovortex production is expected in this environmental situation even though that the genesis of mesovortex is sensitive to storm-scale dynamics. This section investigates the possible mechanisms that lead to the relatively high predictability of mesovortex production with the aid of CTL experiment.

The aforementioned three sensitivity experiments indicate that the probability of mesovortex genesis tends to be high as long as a storm moves through the preexisting triple-point ambient vortex (e.g., Vortex V1 in Fig. 9). However, a relatively long duration of collocation between such a storm and Vortex V1 is also required for the stretching process. For instance, a storm labeled Storm B initiated to the south of Vortex V1 at 1237 BJT and then propagated northeastward across Vortex V1 as shown in Fig. 9c. In the presence of preexisting enhanced ambient vertical vorticity, Storm B developed a well-defined hook echo signature. Nevertheless, it did not manage to develop a mesovortex because it shortly moved away and merged with Storm A. Meanwhile, the ambient Vortex V1 slowly moved toward the southeast (Fig. 12), in a different direction with Storm B, and thus the overlapping time is relatively short.

Although the finger-like echoes failed to wrap up, Storm A still subsequently developed a mesovortex with well-defined mesocyclonic signatures. Through an inspection of the simulated mesocyclonic signature and low-level vertical vorticity, the initial low-level vortex of the midlevel mesovortex was a locally enhanced ambient vortex along the boundary formed by the SE and COF flows (Vortex V2 in Fig. 9). As Storm A approached this boundary, its cold outflows further intensified the convergence and updrafts over Vortex V2 which continuously strengthening the vertical vorticity (Fig. 9). While Vortex V2 also moved in a different direction from the northeastward storm motion (Fig. 12), there was enough time for Vortex V2 to be stretched because the along-boundary length of convective area was relatively long (refer to the heavy black isopleths in Fig. 9). With nearby persistent low-level convective updrafts (Fig. 13a), Vortex V2 was subsequently stretched and finally developed into a midlevel mesovortex (Figs. 4a–c). By contrast, the stronger preexisting triple-point vortex (Vortex V1) failed to be stretched before 1310 BJT due to the lack of low-level updrafts (refer to the dashed rectangle in Fig. 13b). As the western convection approached and thus intensified the upward motions at low levels, the triple-point vortex was gradually enhanced and stretched to form the mesovortex MV-2 (Hook echo B in Fig. 2f) as shown in Figs. 4d–f.

Backward trajectory calculations terminating in the mesovortex at 200 m AGL (refer to the colored lines in Fig. 14a) confirm that the persistent low-level updrafts over Vortex V2 played a key role in the vortex intensification, as low-level stretching was the dominant vorticity-generation term (Fig. 14b). In this study, the backward trajectory calculation was conducted using the RIP (Read/Interpolate/Plot) software package, version 4, that invokes NCAR Graphics routines. Given the 1 min time interval of the WRF outputs, a time step of 10 s was set for trajectory calculation and velocity data were linearly interpolated in time to the trajectory time steps. The time-integrated vertical vorticity generated through vertical stretching ($\zeta\frac{\partial w}{\partial z}$) and tilting ($\xi\frac{\partial w}{\partial x}+\eta\frac{\partial w}{\partial y}$) was calculated along the parcel trajectory. Here ξ, η and ζ represent the components of the vorticity vector at x, y and z directions calculated using the three-dimensional velocity $\vec{V}(u, v, w)$, respectively. Figure 14a shows that the airmasses in the mesovortex originated from the descending air parcels from storms and near-ground ambient air parcels within the southeasterlies over the PRD sea surface. The low-level airmasses from the southeast had higher instability than those from the precipitation regions. Within onshore monsoonal flows, they were initially characterized by high equivalent potential temperature and subsequently underwent a rapid drop of approximately 4 K from ground level to a 200 m altitude during the mixing with the descending air parcels from storms (Fig. 14c).

Although the CTL experiment provides seemingly plausible results, through a dynamic diagnosis, the above analysis suggests "right results but for the wrong reason". The simulated Storm A seemingly has reproduced finger-like echoes, a midlevel mesovortex, and supercell-like structures in rain fields, but with a slightly different mechanism in regard of the detailed genesis process of mesovortex. On storm scales, the simulated finger-like echoes failed to wrap up due to the lack of persistent, strong enough upward motions at low levels near the triple point. The simulated mesovortex originated from the preexisting locally enhanced ambient vortex along surface convergent boundary (Vortex V2). The persistent low-level updrafts along boundary finally prompted the mesovortex formation and the supercell-like structure in the reflectivity field. Similar to the second mesovortex observed by radars (Part I), another simulated mesovortex formed over the triple point zone owing to the arrivals of persistent low-level updrafts associated with the approaching widespread convection (Fig. 3f and Figs. 4d–f).

The simulated Storm B also indicates that a displacement of the triple point and storms, due to their diverged propagating directions (Fig. 9c and Fig. 12), makes it difficult to intensify the preexisting ambient vertical vorticity for developing a midlevel mesovortex. Consequently, although the predictions of rotating storms are sensitive to environmental and storm-scale details at low levels, the simulated and observational facts suggest that a high possibility is expected for an upcoming storm to develop a mesovortex over the triple point that is associated with the land–sea contrast of trumpet-shaped coastline.

5. Summary and discussion

This study is the second part of a two-part series study on the influence of irregular coastlines on a tornadic mesovortex in the Pearl River Delta during monsoon season. In the first part (Part I) of this case study, the prestorm environment on 1 June 2020 was investigated along with the roles of the triple point that is associated with the land–sea contrast of trumpet-shaped coastline on the formation and development of the tornadic storm. The Part I analyses were conducted primarily based on a rapid-scan X-band phased array radar, an S-band operational radar, and in situ surface weather stations. The Part II work presented in the current article was designed to complement the observational analysis of the tornadic mesovortex with the aid of multiple sensitivity numerical simulations.

Twin simulations by using realistic coastline (CTL experiment) and replacing the PRD sea surface with fake land (CTL-land experiment) were conducted to identify the roles played by the trumpet-shaped coastline in the formation of rotating storms in the low-shear environment as well as the intersection of airmass boundaries. The CTL experiment produced two mesovortices near the intersecting zone (triple point) of three types of airmasses (i.e., preexisting storm-generated cold outflows, prevailing monsoonal southwesterlies on land, and sheared monsoonal southeasterlies over the PRD sea surface). Similar to the observed tornadic storm that developed on the triple point, a simulated mesovortex was produced by initially stretching the preexisting ambient vertical vorticity over the triple point. The other simulated mesovortex was produced approximately 6 km to the north of the triple point. It developed from a local maximum of vertical vorticity along the airmass boundary formed by the preexisting storm-generated cold outflows and the sheared monsoonal southeasterlies. The preexisting enhanced ambient vertical vorticity underwent an intensification by the persistent upward motions along the airmass boundary and was stretched to a midlevel mesovortex.

Without fake land in the CTL-land experiment, no triple point was generated due to the absence of land–sea contrast of trumpet-shaped coastline and no rotating storm was produced. The pair of sensitivity simulations suggest that the unique land–sea contrast of PRD is an essential component for the repeatedly occurred enhanced vertical vorticity during the summer monsoon season. The sheared onshore flows over the PRD surface also tend to slow down the eastward propagation of storms.

On storm scales, similar to the observed finger-like echoes, the CTL experiment reproduced well-defined finger-like echoes when the preexisting cold outflow surges intruding into the triple point zone. However, the finger-like echoes were short-lived and did not manage to wrap up as the observed ones did. Another sensitivity experiment (CTL-bubble) was carried out to demonstrate that intensifying the forced lifting associated with the cold outflow surges is a solution to reproduce a mesovortex on the simulated finger-like echoes. In this experiment, the cold outflow surges were artificially strengthened by injecting a cold air volume in the upstream of the finger-like echoes. Fueled by stronger forced lifting, the simulated finger-like echoes successfully wrapped up with a midlevel mesovortex.

Results from the three sensitivity numerical simulations suggest that a high likelihood of rotating storms is expected when preexisting storms juxtapose with the triple point associated with the land–sea contrast of trumpet-shaped coastline. For the short-term probability forecast by convection-permitting modeling, the "correct" result matters even if the detailed storm-scale processes are not perfectly the same after an in-depth post-event investigation. In the current case, the genesis processes of simulated mesovortex are not completely consistent with the scenario suggested by multi-source observations, the simulations have provided important guidance for this tornadic event that occurs in a low-shear environment. The discrete vortices transformed from the vortex sheet associated with the airmass boundary via shear instability play an important role in the relatively high predictability of mesovortex production (Markowski et al. 2014). The presence of multiple local maxima in vertical vorticity both over the triple point and along the airmass boundary increases the risk of rotating storms which may spawn tornadoes even in the dynamic conditions with low vertical wind shear. Compared to the along-boundary preexisting ambient vortex, the triple-point vortex is believed to have a higher possibility for an upcoming storm to organize into a rotating storm because of the stronger vertical vorticity in that region. Such a possibility would be even higher when the storm propagates along the preexisting boundary, especially when the long axis of the storm is also generally parallel to the boundary. In this situation, the low-level convective updrafts tend to overlap with the triple-point vortex with a relatively long duration for stretching.

Tornado statistics have showed that the PRD is a tornado-prone region. Although it is still not clear that how many tornadoes are associated with such nonmesocyclone processes, the current study suggests that the topography-related localized ambient vertical vorticity that results from storm-boundary interaction is probably an important component for the formation of rotating storms in this region. It should be noted that this mechanism is conspicuous during the monsoon active season when the PRD region is characterized by prevailing southwesterlies in the lower troposphere. More in-depth case studies are warranted to better understand the prominent regional formation mechanisms of tornadic storms, which would greatly support the local severe weather forecast over this tornado hotspot.

Acknowledgments. This study was supported by the National Natural Science Foundation of China (42275006, U2242203 and 42030604), the Guangdong Basic and Applied Basic Research Foundation (2023A1515011705 and 2021A1515011647), and the Science and Technology Research Project for Society of Foshan (2120001008761). The reanalysis data used for this article can be accessed on the European Centre for Medium-Range Weather Forecasts (ECMWF) website (https://cds.climate.copernicus.eu/cdsapp#!/dataset/reanalysis-era5-pressure-levels?tab=form). The authors are grateful for the helpful reviews provided by the editors and anonymous reviewers.

REFERENCES

Bai, L., Z. Meng, K. Sueki, G. Chen, and R. Zhou, 2020: Climatology of tropical cyclone tornadoes in China from 2006 to 2018. *Science China Earth Sciences*, 63, 37–51. https://doi.org/10.1007/s11430-019-9391-1

Bai, L., Z. Meng, D. Yao, Y. Zhang, X. Huang, Z. Li, X. Yu, 2023: Influence of irregular coastlines on a tornadic mesovortex in the Pearl River Delta during monsoon season. Part I: Prestorm environment and storm evolution. *Advances in Atmospheric Sciences*, conditional accepted.

Bluestein, H. B., 1985: The formation of a “landspout” in a “broken-line” squall line in Oklahoma. Preprints, 14th Conf. on Severe Local Storms, Indianapolis, IN, *Amer. Meteor. Soc*., 267–270.

Bryan, G., J. Fritsch, 2002: A benchmark simulation for moist nonhydrostatic numerical models. *Monthly Weather Review*, 130, 2917–2928. https://doi.org/10.1175/1520-0493(2002)130<2917:ABSFMN>2.0.CO;2

Burgess, D. W., R. J. Donaldson Jr., and P. R. Desrochers, 1993: Tornado detection and warning by radar. The Tornado: Its Structure, Dynamics, Prediction, and Hazards, Geophys. Monogr., No. 79, *Amer. Geophys. Union*, 203–221.

Caruso, J. M., and J. M Davies., 2005: Tornadoes in nonmesocyclone environments with pre-existing vertical vorticity along convergence boundaries. *NWA Electron. J. Operational Meteorology*, 6, 1–36. [Available online at http://www.nwas.org/ej/pdf/2005-EJ4.pdf]

Chou, M., and M. Suarez, 1994: An efficient thermal infrared radiation parameterization for use in general circulation models (NASA Technical Memorandum, p. 84). NASA.

Davies, J. M., 2006: Tornadoes in Environments with Small Helicity and/or High LCL Heights. *Wea. Forecasting*, 21, 579–594. https://doi.org/10.1175/WAF928.1

Fan, W. and Yu, X., 2015: Characteristics of spatial-temporal distribution of tornadoes in China (in Chinese with English abstract). *Meteor. Mon.*, **41**, 793–805.

Hersbach, H., and Coauthors, 2020: The ERA5 global reanalysis. *Quart. J. of the Royal Meteorological Society*, 146, 1999–2049. https://doi.org/10.1002/qj.3803

Hong, S. Y., and Lim, J. J., 2006: The WRF single-moment 6-class microphysics scheme (WSM6). *Journal of the Korean Meteorological Society*, 42(2), 129–151.

Houston, A. L., and R. B. Wilhelmson, 2007a: Observational Analysis of the 27 May 1997 Central Texas Tornadic Event. Part I: Prestorm Environment and Storm Maintenance/Propagation. *Monthly Weather Review*, 135, 701–726. https://doi.org/10.1175/MWR3300.1

Houston, A. L., and R. B. Wilhelmson, 2007b: Observational Analysis of the 27 May 1997 Central Texas Tornadic Event. Part II: Tornadoes. *Monthly Weather Review*, 135, 727–735. https://doi.org/10.1175/MWR3301.1

Kain, J. S., and Coauthors, 2008: Some Practical Considerations Regarding Horizontal Resolution in the First Generation of Operational Convection-Allowing NWP. Weather and Forecasting, 23, 931–952, https://doi.org/10.1175/WAF2007106.1

Lee, B. D., and R. Wilhelmson, 1997a: The numerical simulation of nonsupercell tornadogenesis. Part I: Initiation and evolution of pretornadic misocyclone circulations along a dry outflow boundary. *Journal of the Atmospheric Sciences*, 54, 32–60, https://doi.org/10.1175/1520-0469(1997)054<0032:TNSONS>2.0.CO;2

Lee, B. D., and R. Wilhelmson, 1997b: The numerical simulation of nonsupercell tornadogenesis. Part II: Evolution of a family of tornadoes along a weak outflow boundary. *Journal of the Atmospheric Sciences*, 54, 2387–2414, https://doi.org/10.1175/1520-0469(1997)054<2387:TNSONT>2.0.CO;2

Lemon, L. R., and C. A. Doswell III, 1979: Severe thunderstorm evolution and mesocyclone structure as related to tornadogenesis, *Monthly Weather Review*, 107, 1184–1197.

Markowski, P. M., 2002: Hook echoes and rear-flank downdrafts: A review. *Monthly Weather Review*, 130, 852–876. https://doi.org/10.1175/1520-0493(2002)130<0852:Hearfd>2.0.Co;2

Markowski, P., Y. Richardson, and G. Bryan, 2014: The Origins of Vortex Sheets in a Simulated Supercell Thunderstorm. *Monthly Weather Review*, 142, 3944–3954. https://doi.org/10.1175/MWR-D-14-00162.1

Markowski, P., 2020: What is the Intrinsic Predictability of Tornadic Supercell Thunderstorms? Monthly Weather Review, 148, 3157–3180. https://doi.org/10.1175/MWR-D-20-0076.1

Mlawer, E. J., S. J. Taubman, P. D. Brown, M. J. Iacono, and S. A. Clough, 1997: Radiative transfer for inhomogeneous atmospheres: RRTM, a validated correlated-k model for the longwave. *J. Geophys. Res.*, 102, 16663–16682. https://doi.org/10.1029/97JD00237

Noh, Y., W. Cheon, S. Hong, and S. Raasch, 2003: Improvement of the K-profile model for the planetary boundary layer based on large eddy simulation data. *Boundary-Layer Meteor.*, 107, 401–427. https://doi.org/10.1023/A:1022146015946

Orlanski, I., 1975. A rational subdivision of scales for atmospheric processes. *Bull. Am. Meteorol. Soc.,* 56, 527–530.

Rasmussen, E. N., 2003: Refined supercell and tornado forecast parameters. *Wea. Forecasting*, 18, 530–535.

Schenkman, A. D., and M. Xue, 2016: Bow-echo mesovortices: A review. *Atmospheric Research*, 170, 1–13. https://doi.org/10.1016/j.atmosres.2015.11.003

Schenkman, A. D., M. Xue, and A. Shapiro, 2012: Tornadogenesis in a Simulated Mesovortex within a Mesoscale Convective System. *Journal of the Atmospheric Sciences*, 69, 3372–3390. https://doi.org/10.1175/JAS-D-12-038.1

Skamarock, W. C., and Coauthors, 2008: A description of the Advanced Research WRF version 3. NCAR Tech. Note NCAR/TN-475+STR, 113 pp. [Available online at http://www.mmm.ucar.edu/wrf/users/docs/arw_v3_bw.pdf]

Wakimoto, R. M., and J. W. Wilson, 1989: Non-supercell Tornadoes. *Monthly Weather Review*, 117, 1113–1140. https://doi.org/10.1175/1520-0493(1989)117<1113:NST>2.0.CO;2

Wang, P., 1996: On environmental conditions of the genesis of tornado in the Zhujiang river delta in spring, *Journal of Tropical Meteorology*, 2, 98–103.

Yu, X., and Z. Yongguang, 2020: Advances in severe convection research and operation in China. *Journal of Meteorological Research*, 34, 189–217.

Zhang, Y., L. Bai, Z. Meng, B. Chen, C. Tian, and P. Fu, 2021: Rapid-scan and polarimetric phased-array radar observations of a tornado in the Pearl River Estuary. *Journal of Tropical Meteorology*, **27**, 80–85. https://doi.org/10.46267/j.1006-8775.2021.008

Zhou, R., Z. Meng, and L. Bai, 2021: Differences in Tornado Activities and Key Tornadic Environments between China and the United States. *International J. Climatology*, **42**, 1–18. https://doi.org/10.1002/joc.7248

Zhou, R., Z. Meng, and L. Bai, 2020: Tornado Database in China (2007~2016), Peking University Open Research Data Platform. https://doi.org/10.18170/DVN/QKQHTG

FIGURES

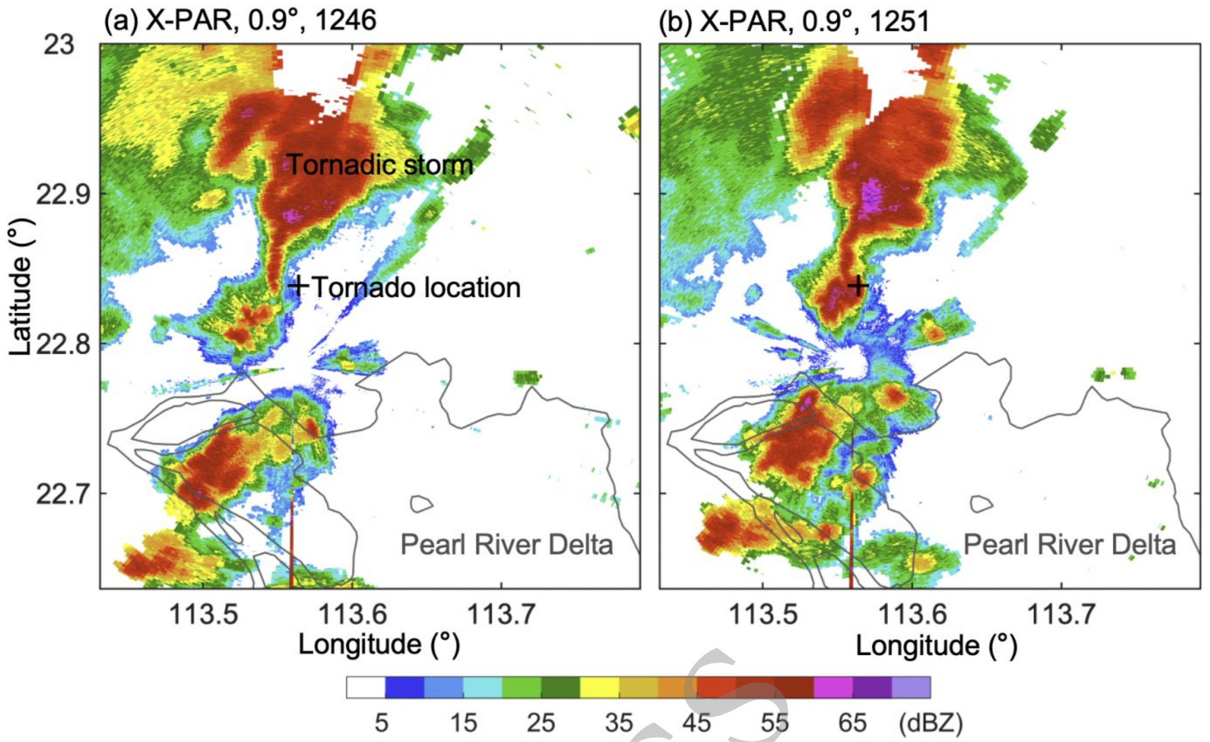

Fig. 1. Reflectivity obtained from the Nansha X-band phased-array (X-PAR) radar at the 0.9° elevation angle at (a) 1246 BJT and (b) 1251 BJT on 1 June 2020. The black cross represents the reported tornado location.

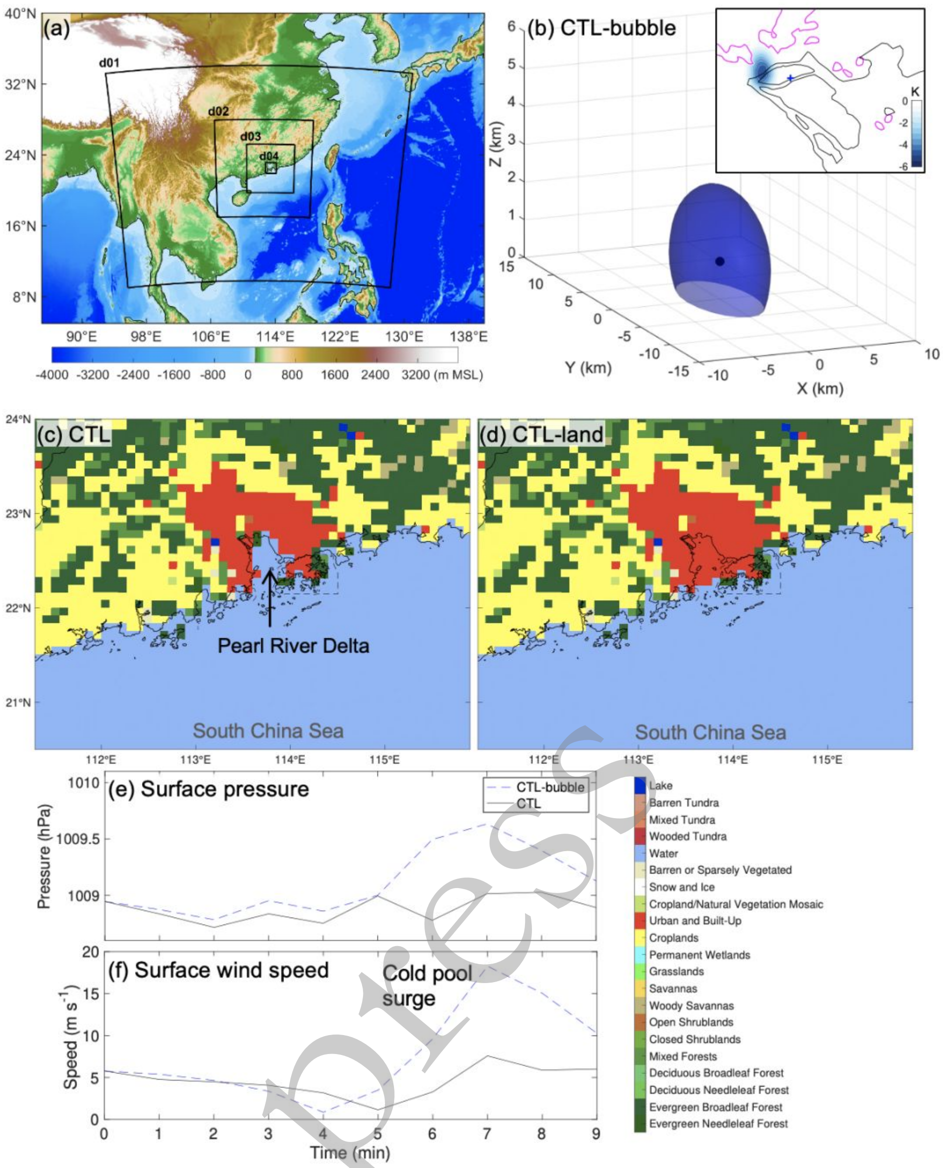

Fig. 2. (a) WRF domain configuration with terrain heights (shadings). (b) Schematic of the injected localized volume of negatively buoyant air in the CTL-bubble sensitivity simulation. This cool bubble was placed (22.7544°N, 113.455°E) to the west of the simulated finger-like echoes of Storm A as shown in (Fig. 10b) at 1220 BJT. The difference of near-surface temperature between the CTL-bubble and CTL experiments at 1221 BJT is also shown in the upper-right corner for reference. Reflectivity on model level 5 is contoured at 40 dBZ in magenta. It is centered at a height of 1 km with a horizontal radius of 10 km and a vertical radius of 1.5 km above ground. The potential temperature perturbation was minimized at the center with a minimum perturbation of −10 K and increased to 0 K following a cosine function over a radius of 3.5 km, 6 km and 2 km in the zonal, meridional and vertical directions, respectively. (c) Land use types of the CTL experiment that represents the realistic topography (interpolated from the outermost WRF domain) and (d) the CTL-land experiment in which the PRD sea surface is replaced by land surface. Time series of (e) surface pressure and (f) surface wind speeds for the CTL-bubble (blue) and CTL (black) experiments are plotted since 1220 BJT. The selected location is marked by the cross as shown in the inset of (b).

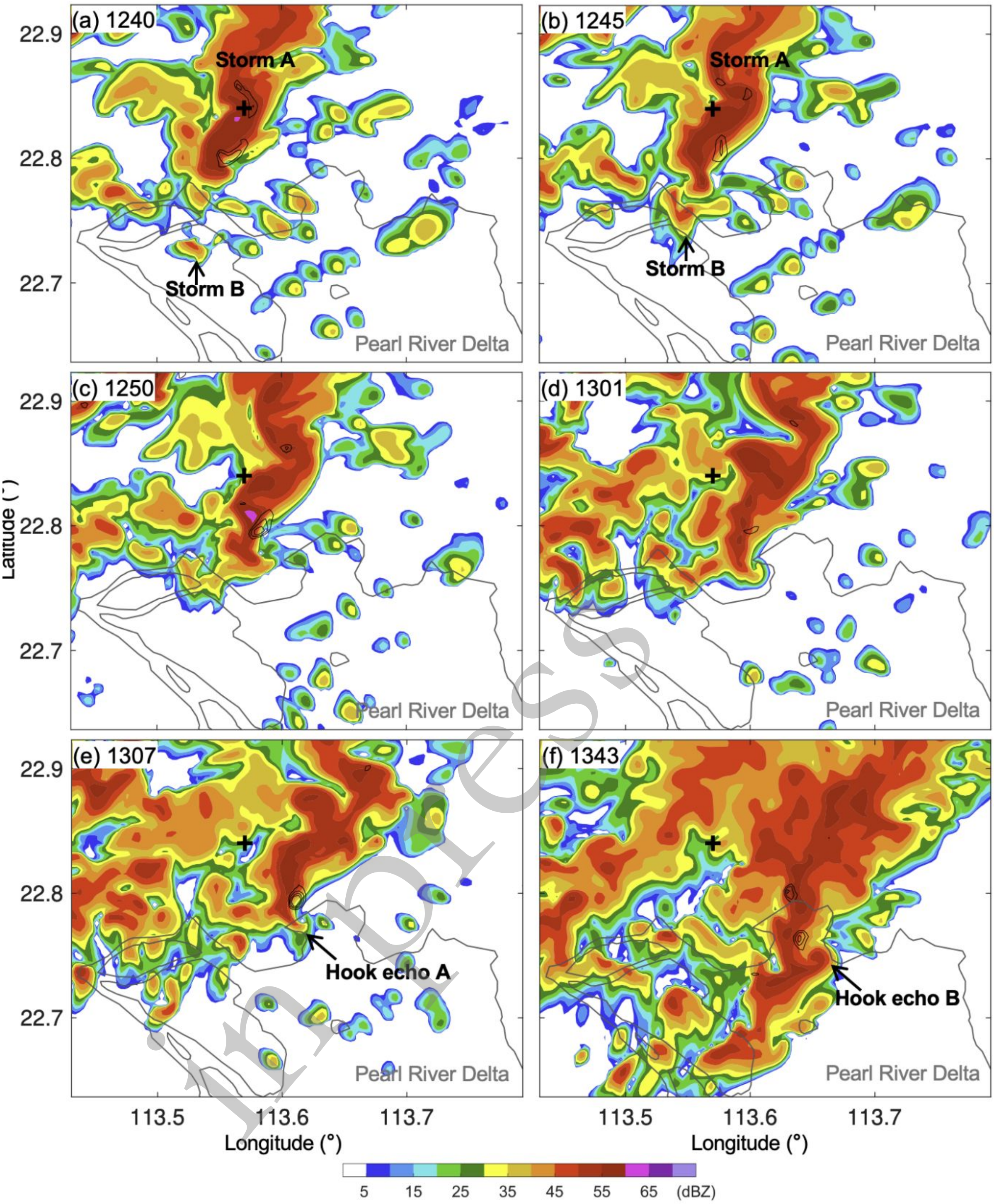

Fig. 3. Simulated reflectivity on the level 5 (approximately 300 m above ground) at different times (BJT) showing the modeled storm evolutions provided by the CTL experiment. The updraft helicity is contoured in black from 400 $m^2 s^{-2}$ at an interval of 200 $m^2 s^{-2}$. The black cross denotes the approximate location of the observed tornado.

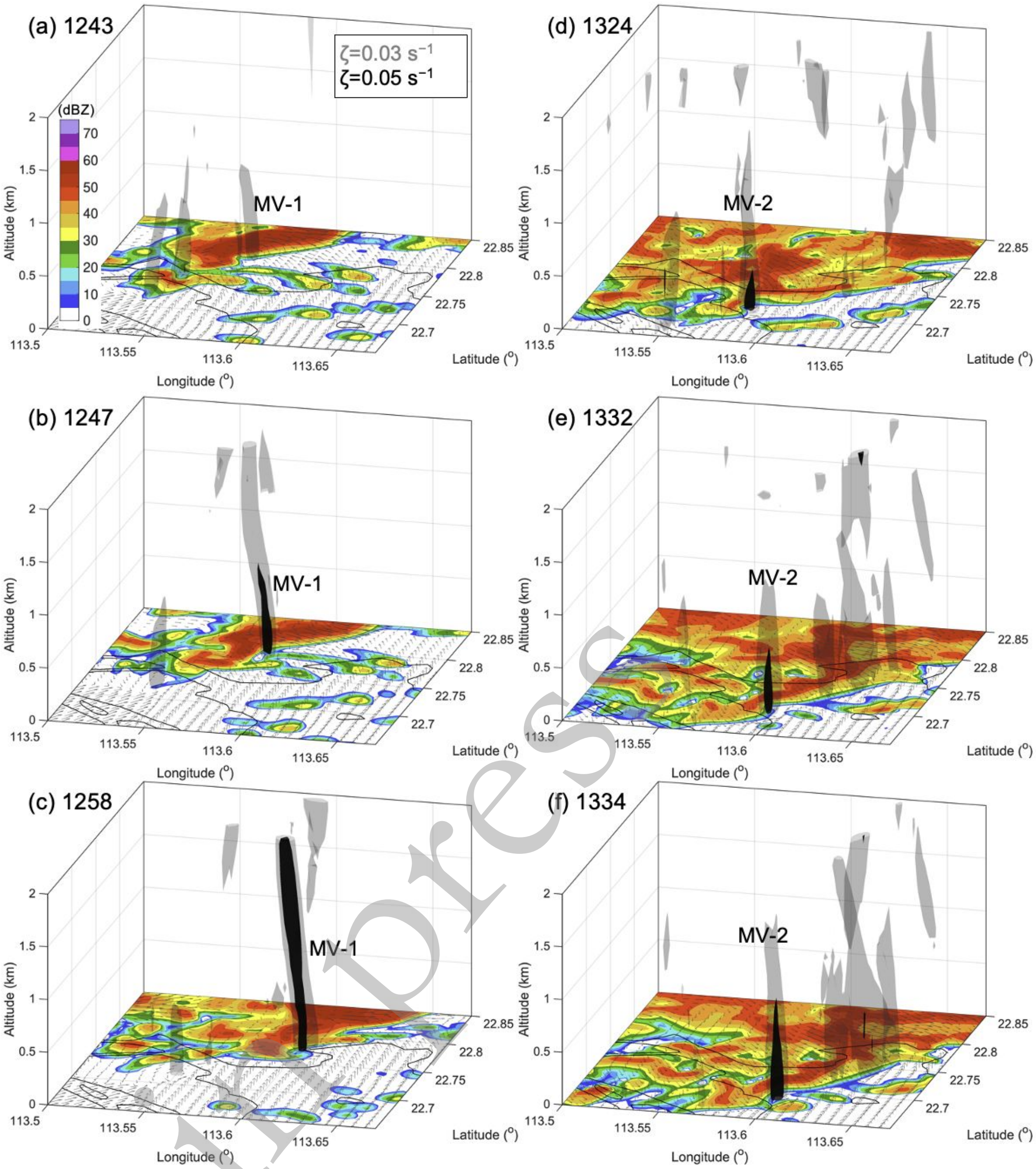

Fig. 4. Three-dimensional isosurfaces of 0.03 s^{-1} (gray) and 0.05 s^{-1} (black) vertical vorticity valid at different times (BJT) on 1 June 2020 from WRF d04 simulations. The simulated reflectivity and horizontal winds at the model level 5 above ground are also shown at the bottom for reference. The columns of enhanced vertical vorticity labeled MV-1 and MV-2 represent the mesovortices described in the text.

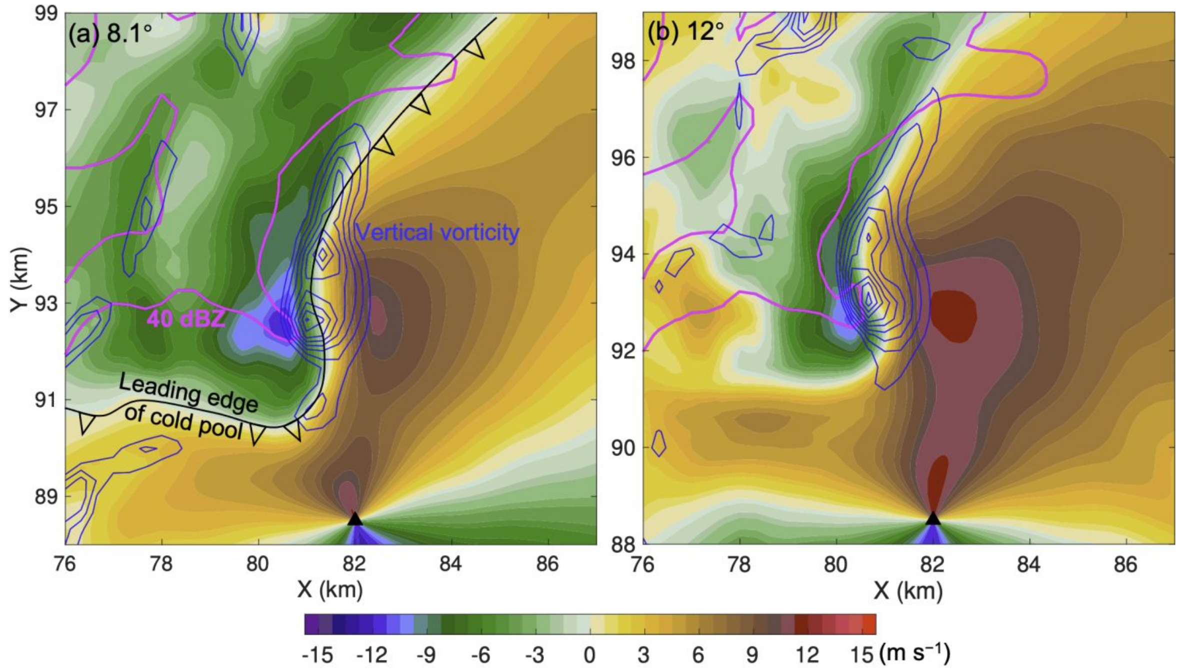

Fig. 5. Simulated radial velocity and reflectivity at the (a) 8.1° and (b) 12° elevation angle from the virtual radar (black triangle) at 1301 BJT. Reflectivity is contoured at 40 dBZ in magenta. The vertical vorticities at (a) level 3 and (b) level 8 above ground are contoured in blue from 0.005 s^{-1} at an interval of 0.004 s^{-1}. The outflow boundary in (a) appears as a curve with triangles.

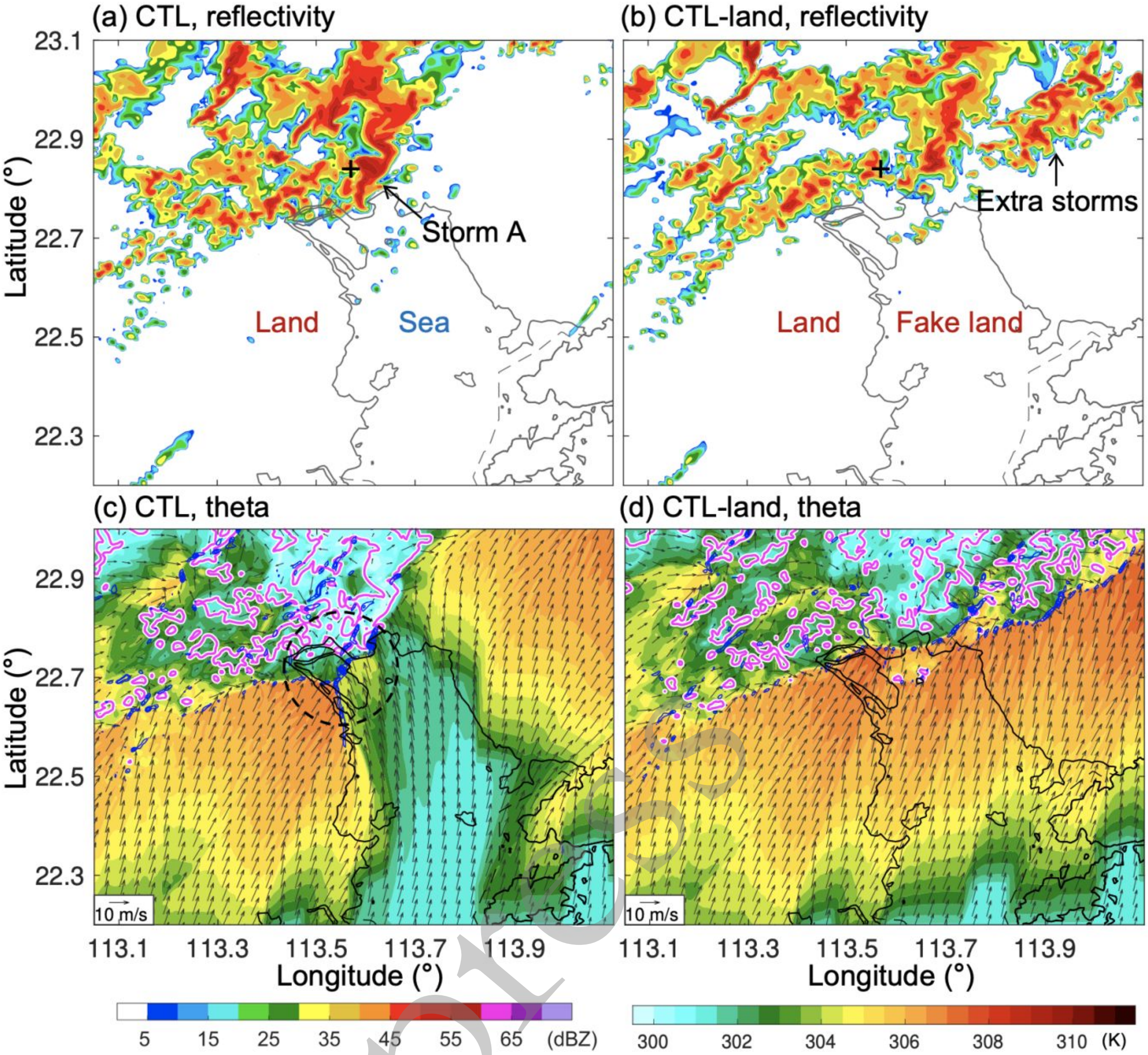

Fig. 6. Comparisons of the simulated reflectivity on the model level 5 at 1300 BJT on 1 June between the (a) CTL and (b) CTL-land experiments. Comparisons of the simulated potential temperature (shaded) and horizontal winds (vectors) on the model level 3 at that time are presented in (c) and (d). The simulated reflectivity is contoured at 40 dBZ in magenta. Vertical vorticity is contoured from 0.005 s^{-1} at an interval of 0.004 s^{-1} in blue. The dashed circle in (c) marks the location of triple-point zone.

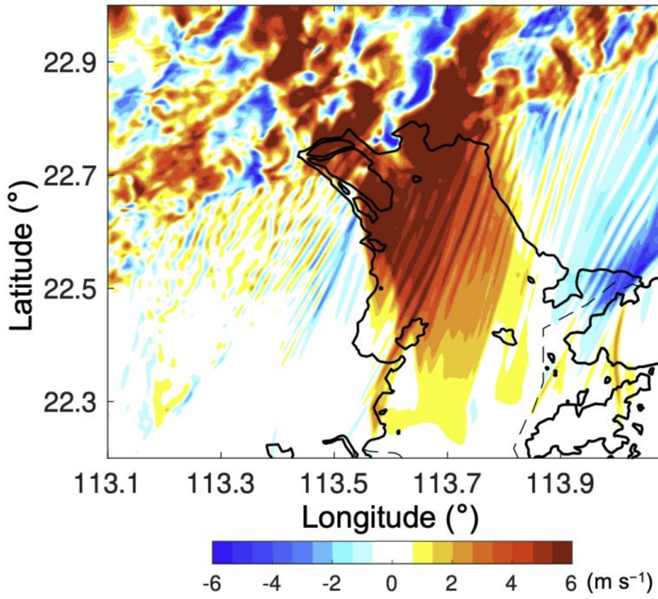

Fig. 7. Differences of the *u*-wind components on the lowest model level at 1300 BJT on 1 June between the CTL-land and the CTL experiments.

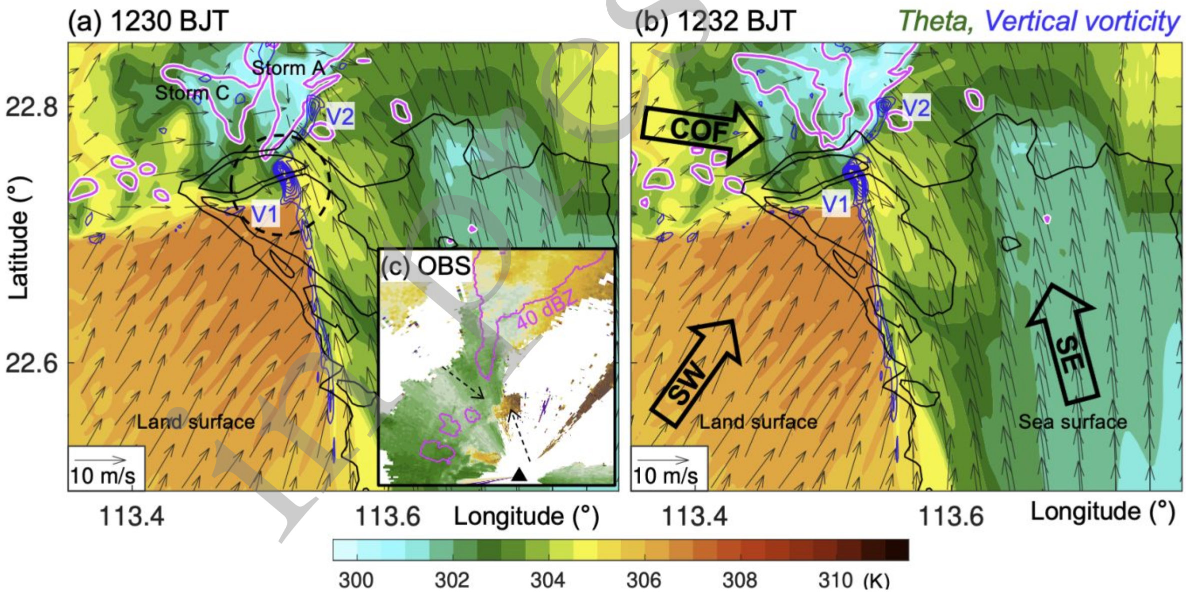

Fig. 8. (a),(b) Potential temperature (shaded) and horizontal winds (vectors) on the model level 3 above ground. The vortical vorticity on this level is contoured from 0.005 s^{-1} at an interval of 0.004 s^{-1} in blue and the reflectivity is contoured at 40 dBZ in magenta. The dashed circle in (a) marks the location of triple-point zone. Vertical vorticity maxima are labeled V1 and V2, respectively. The panel (c) in the bottom-left corner of (a) shows the observed radial velocity (shaded; color scales are the same as that in Fig. 5) and reflectivity (magenta) at the 0.9° elevation angle of X-PAR at 1245 BJT on 1 June 2020.

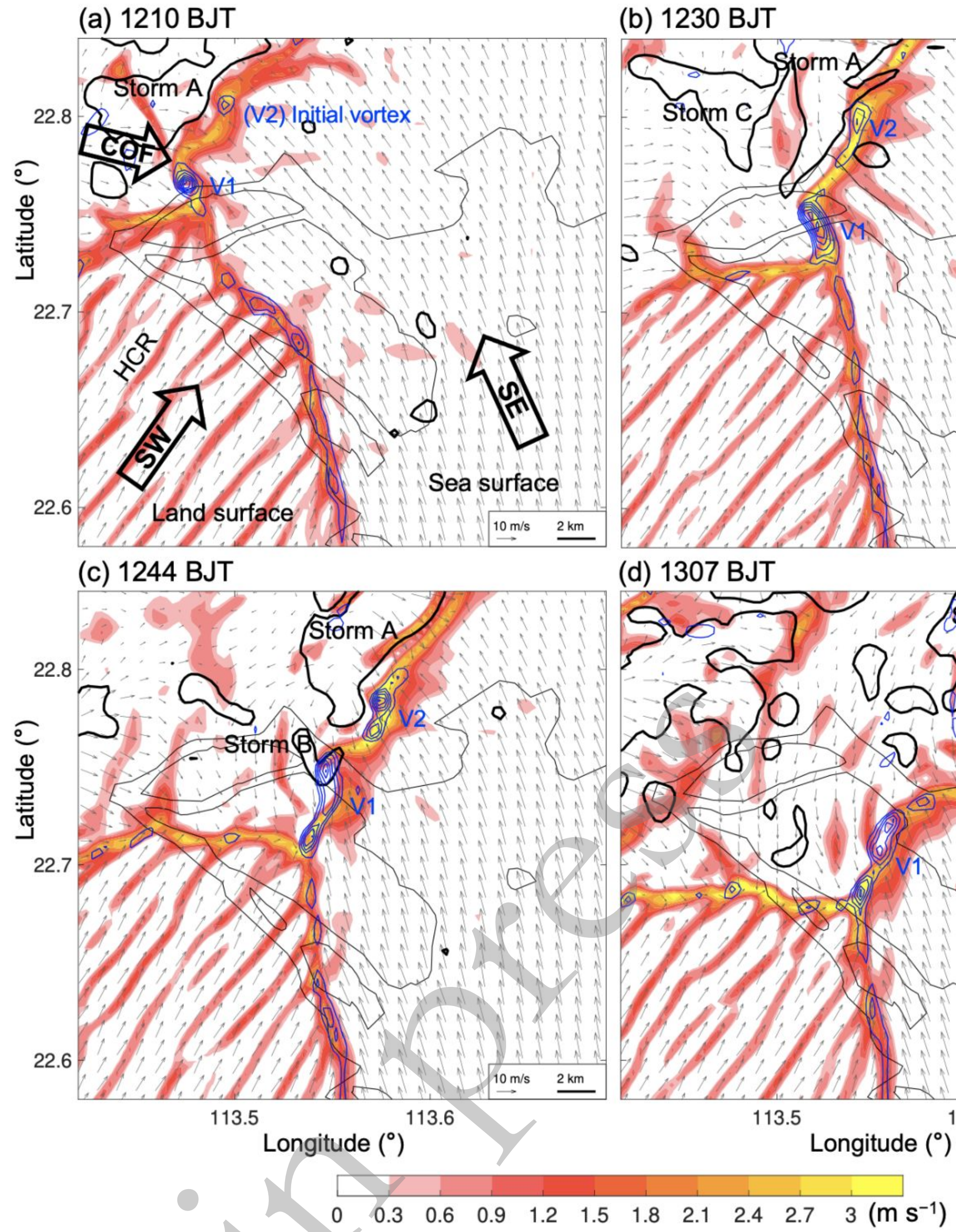

Fig. 9. Vertical velocity (shaded) and horizontal winds (vectors) on the model level 3 above ground. The simulated reflectivity is contoured at 40 dBZ (heavy black isopleths) and the vortical vorticity is contoured from 0.005 s^{-1} at an interval of 0.004 s^{-1} in blue. The enhanced vertical vorticity zones are labeled V1 and V2.

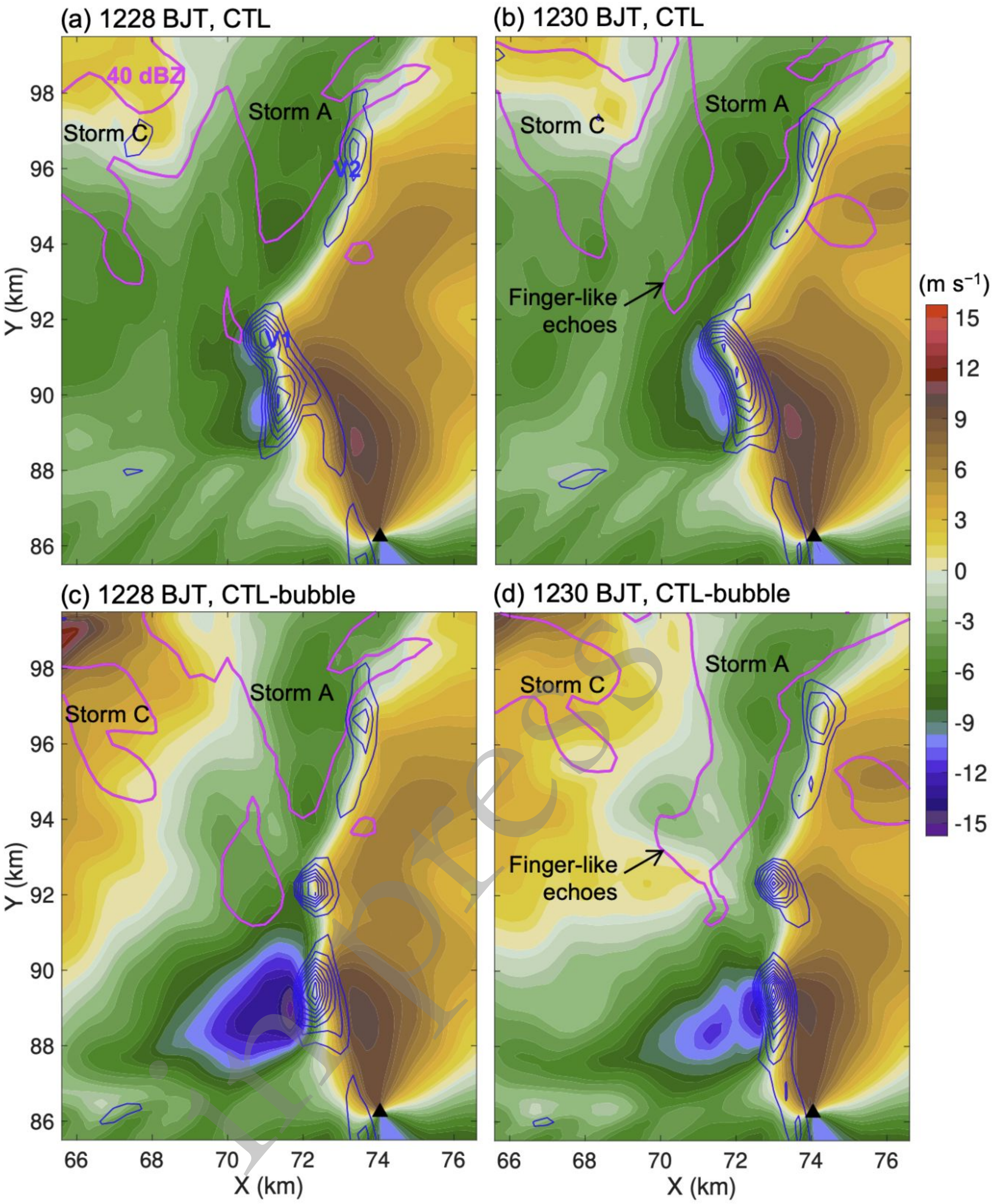

Fig. 10. Simulated radial velocity at the 8.1° elevation angle from the virtual X-PAR (black triangle) for the (top) CTL and (bottom) CTL-bubble experiments. The reflectivity is contoured at 40 dBZ in magenta. The vertical vorticity at level 3 above ground is contoured in blue from 0.005 s^{-1} at an interval of 0.004 s^{-1}.

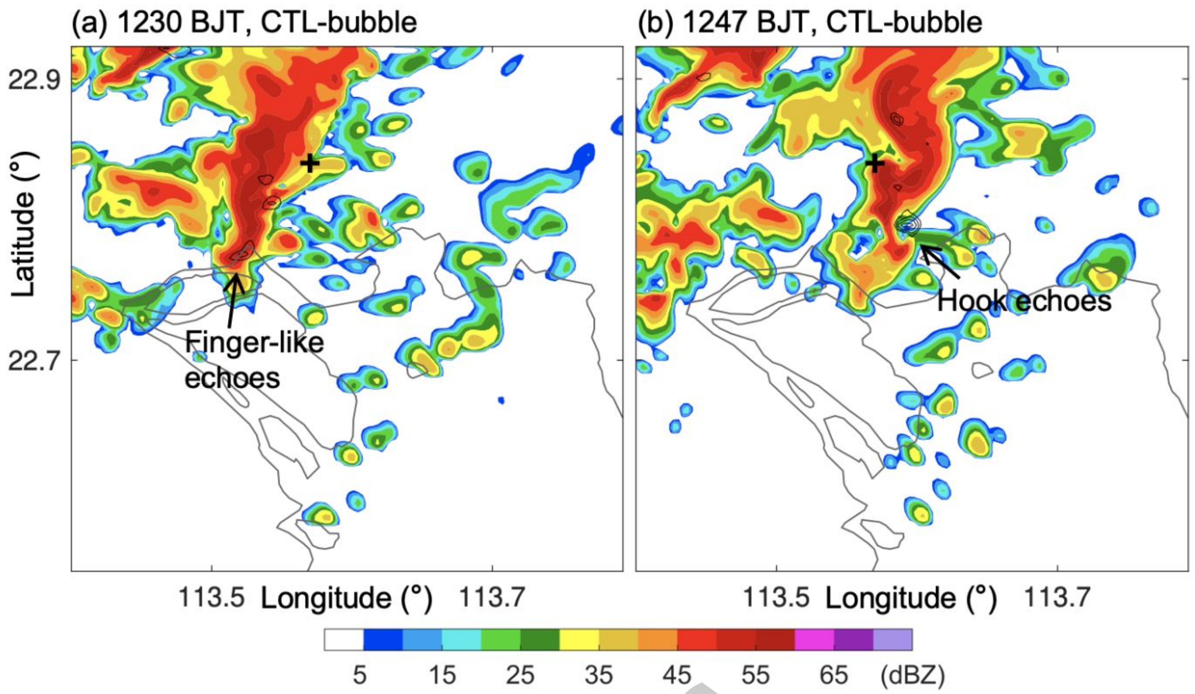

Fig. 11. Same as Fig. 3 but for the CTL-bubble experiment.

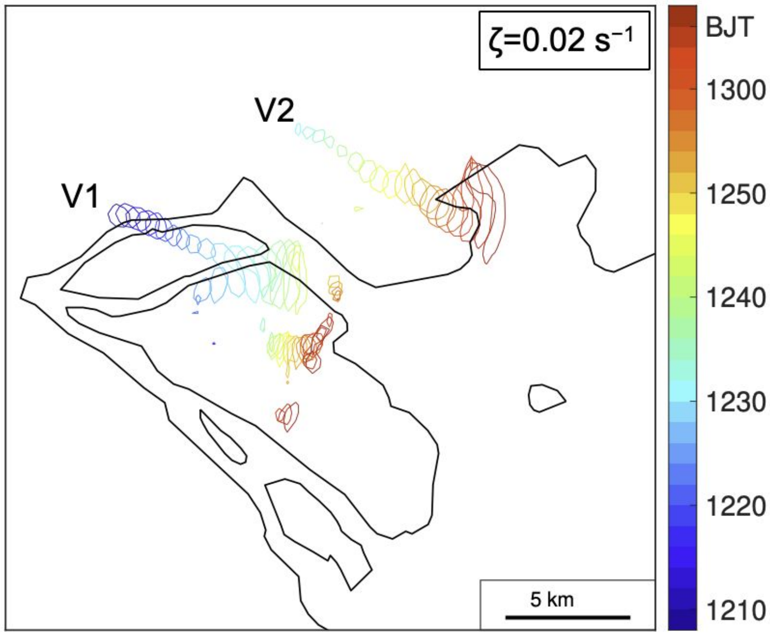

Fig. 12. Vertical vorticity isopleths of 0.02 s^{-1} (isopleths) on the model level 3 above ground calculated from the innermost domain of the CTL experiment on 1 June 2020. The colors represent different times on that day.

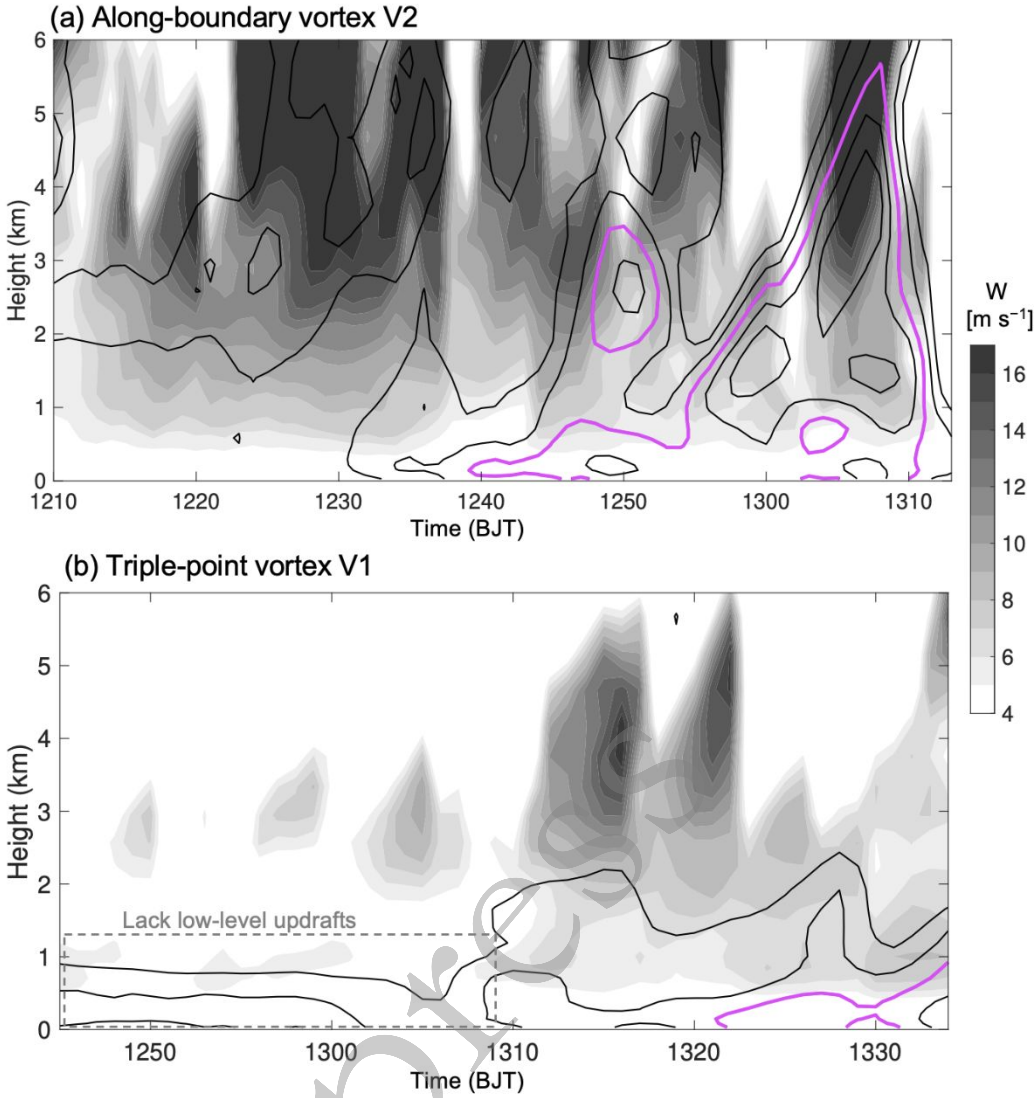

Fig. 13. Time–height diagrams of peak vertical vorticity (contoured from 0.015 s^{-1} at an interval of 0.005 s^{-1}; the isopleth of 0.025 s^{-1} is highlighted in magenta) maximized on each level over the (a) along-boundary vortex V2 and (b) triple-point vortex V1 as shown in Fig. 9. The gray shadings represent the maximum vertical velocity within 2 km of the location of peak vertical vorticity. The dashed box in (b) is described in the text. All variables are calculated from the innermost domain of the CTL experiment on 1 June 2020.

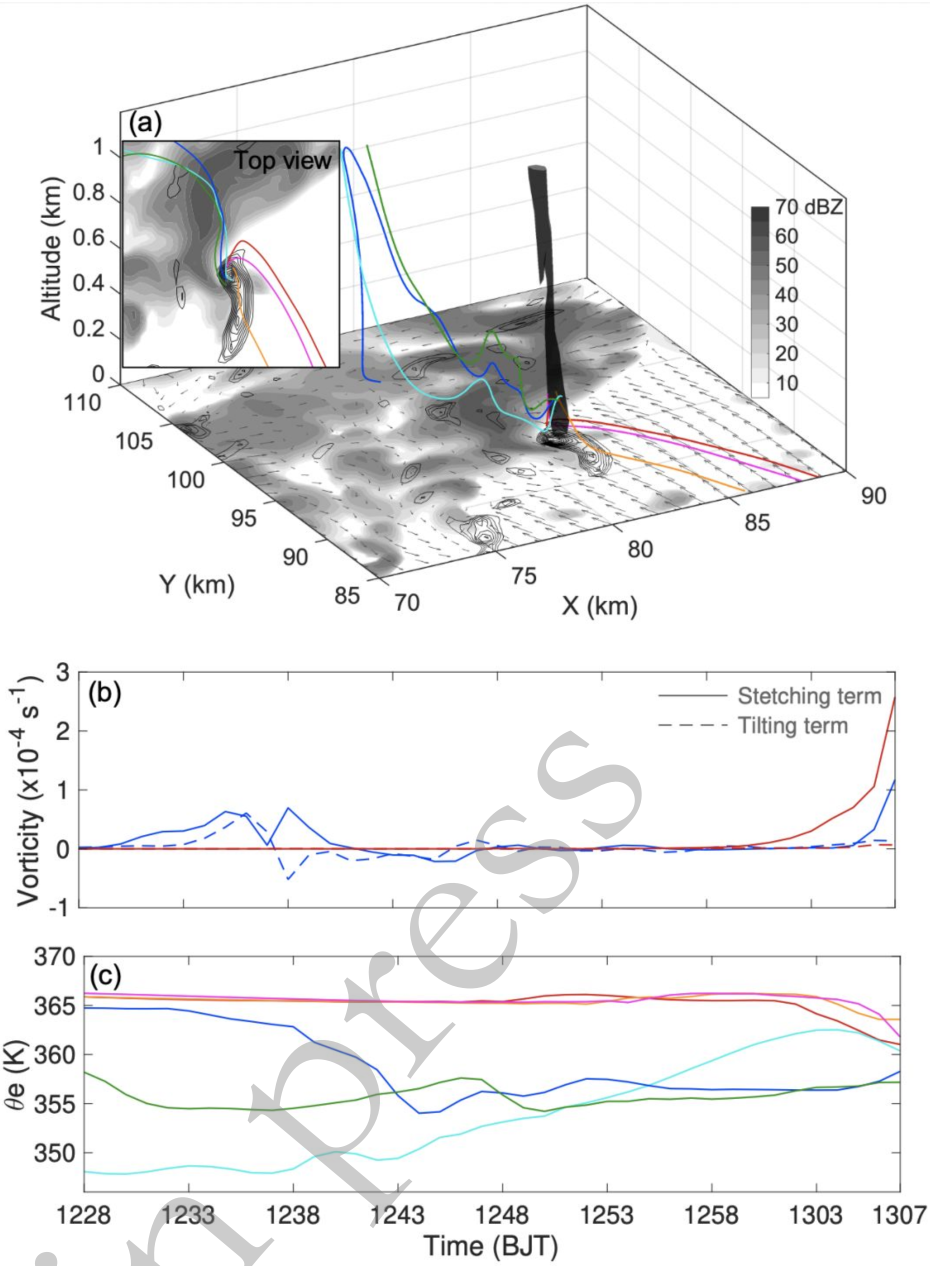

Fig. 14. (a) Three-dimensional isosurfaces (black column, 0.025 s^{-1}) of vertical vorticity at 1307 BJT on 1 June 2020. The simulated reflectivity (shaded in gray), vortical vorticity (black isopleths, contoured from 0.005 s^{-1} at an interval of 0.004 s^{-1}), and horizontal winds (vectors) on the model level 5 above ground are also shown at the bottom for reference. Several backward trajectories terminated at 200 m altitude around the enhanced vortical vorticity are plotted by colored curves. A top view is also presented in the upper-left corner. (b) Vertical vorticity tendency for the air parcels marked by the red and blue lines in (a) with corresponding line colors. The stretching and tilting terms are represented by solid and dashed lines, respectively. (c) Equivalent potential temperature for the air parcels in (a) with corresponding line colors. All variables are calculated from the innermost domain of the CTL experiment on 1 June 2020.